SUPPLEMENT

STATE OF THE CLIMATE IN 2013

Supplemental Figures

JESSICA BLUNDEN AND DEREK S. ARNDT, EDS.

This document is a supplement to *State of the Climate in 2013,* Jessica Blunden and Derek S. Arndt, Eds. [*Bull. Amer. Meteor. Soc.,* **95** (7), S1–S257] • ©2014 American Meteorological Society • DOI:10.1175/2014BAMSStateoftheClimate.2

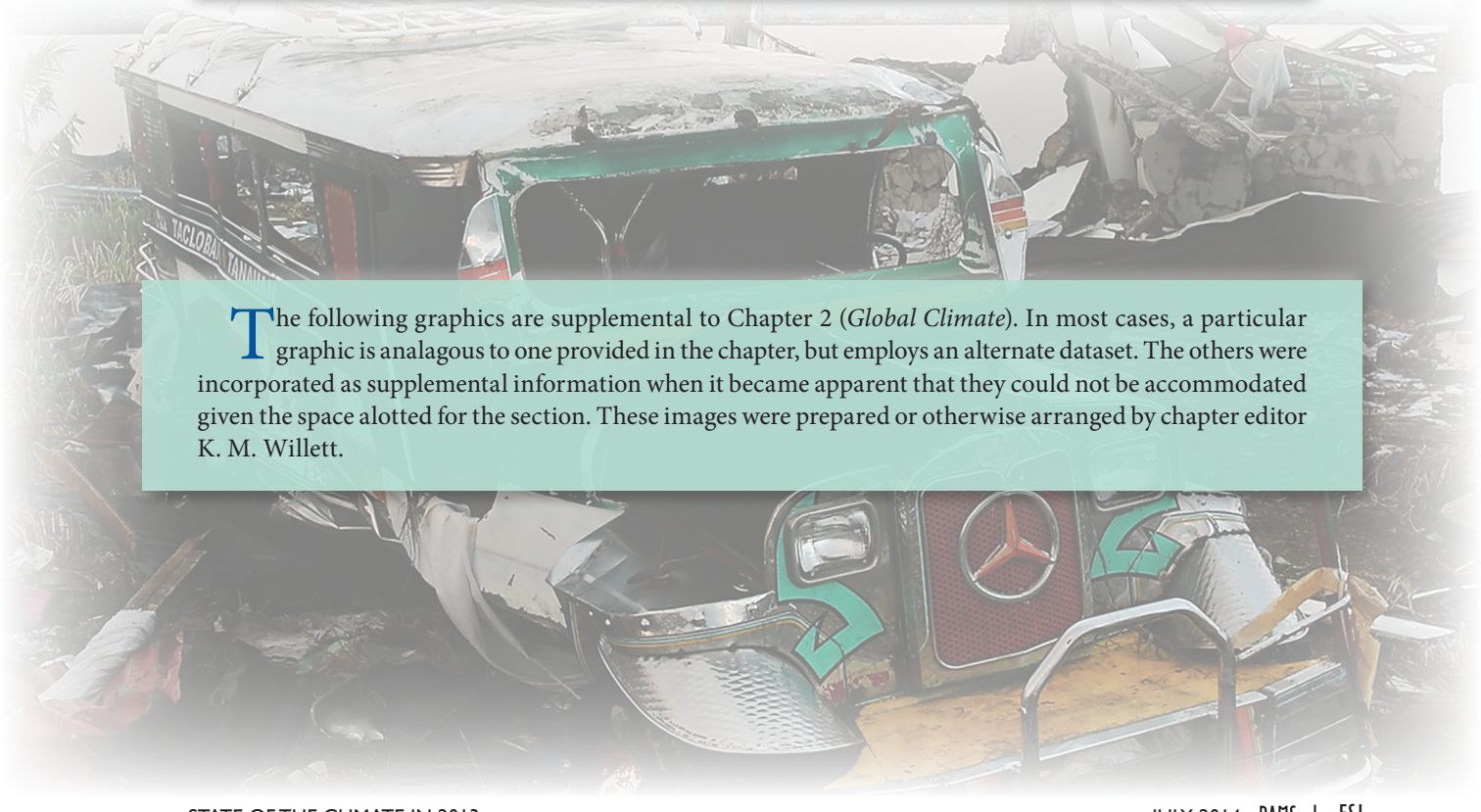

The following graphics are supplemental to Chapter 2 (*Global Climate*). In most cases, a particular graphic is analagous to one provided in the chapter, but employs an alternate dataset. The others were incorporated as supplemental information when it became apparent that they could not be accommodated given the space alotted for the section. These images were prepared or otherwise arranged by chapter editor K. M. Willett.

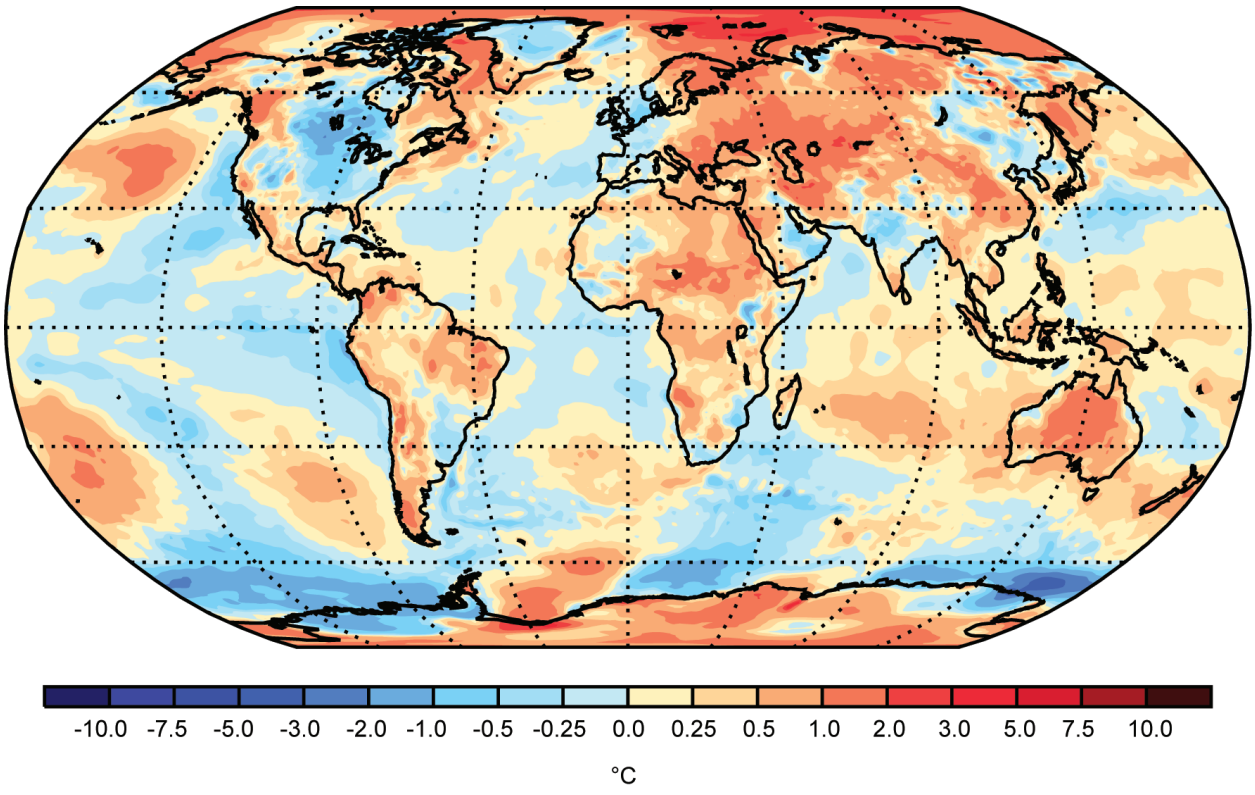

Fig. S2.1. ERA-Interim 2013 annual anomaly map of surface (2-m) temperature (°C; 1981–2010 base period).

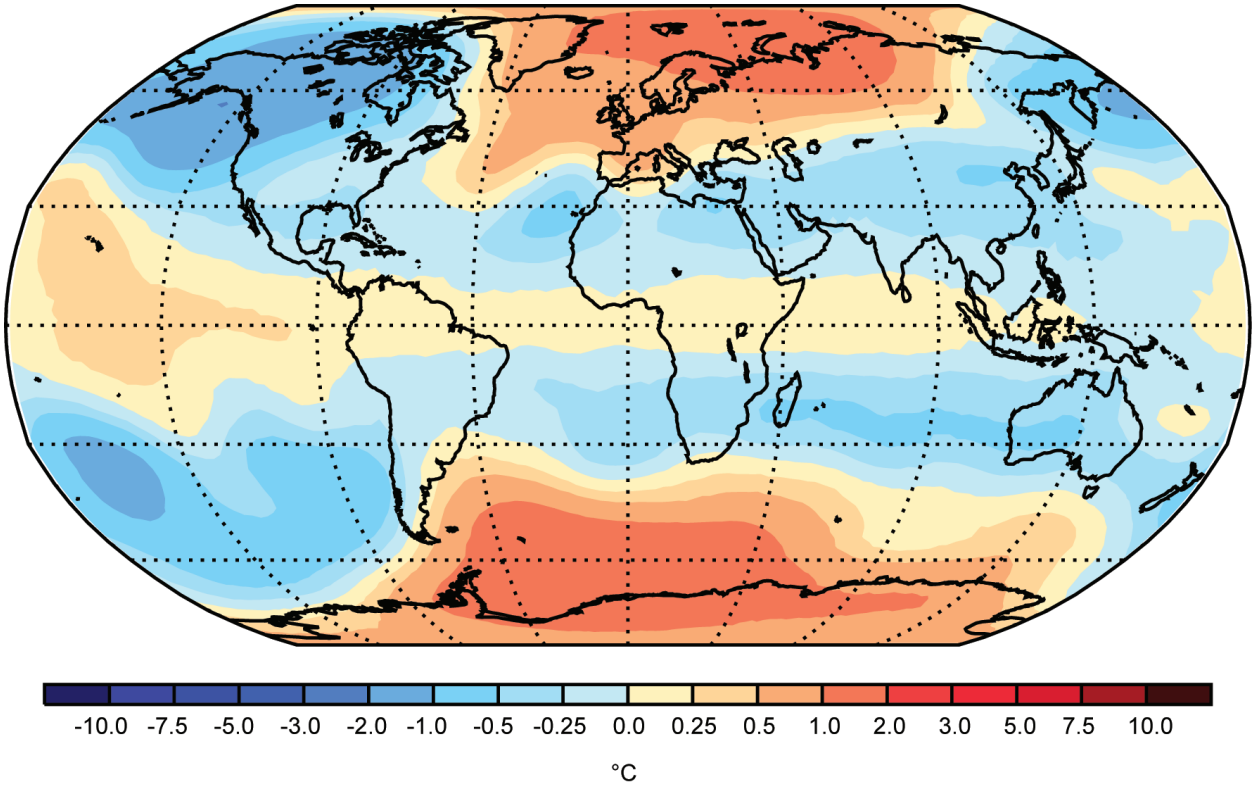

Fig. S2.2. MERRA 2013 annual anomalies (°C; 1981–2010 base period) of MSU channel 4 equivalent layer for the lower stratospheric temperature.

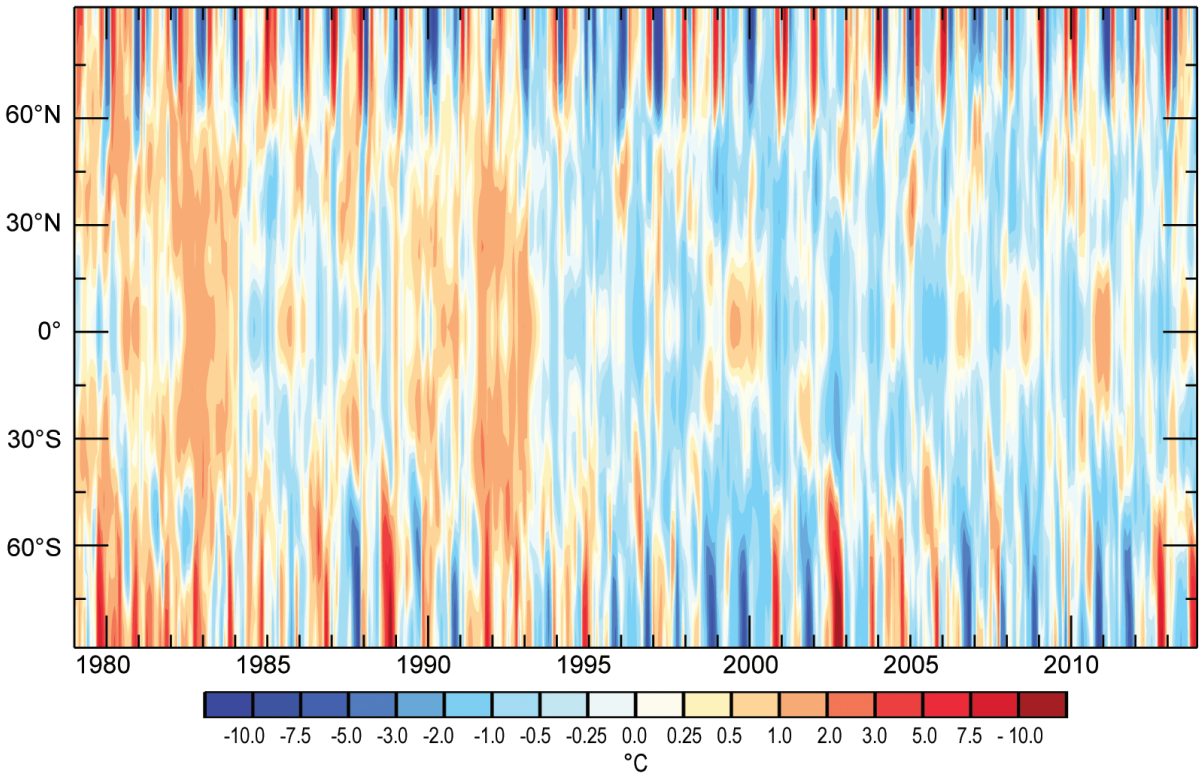

Fig. S2.3. MERRA monthly mean anomalies (°C; 1981–2010 base period) of lower stratospheric temperature MSU Channel 4 equivalent by latitude.

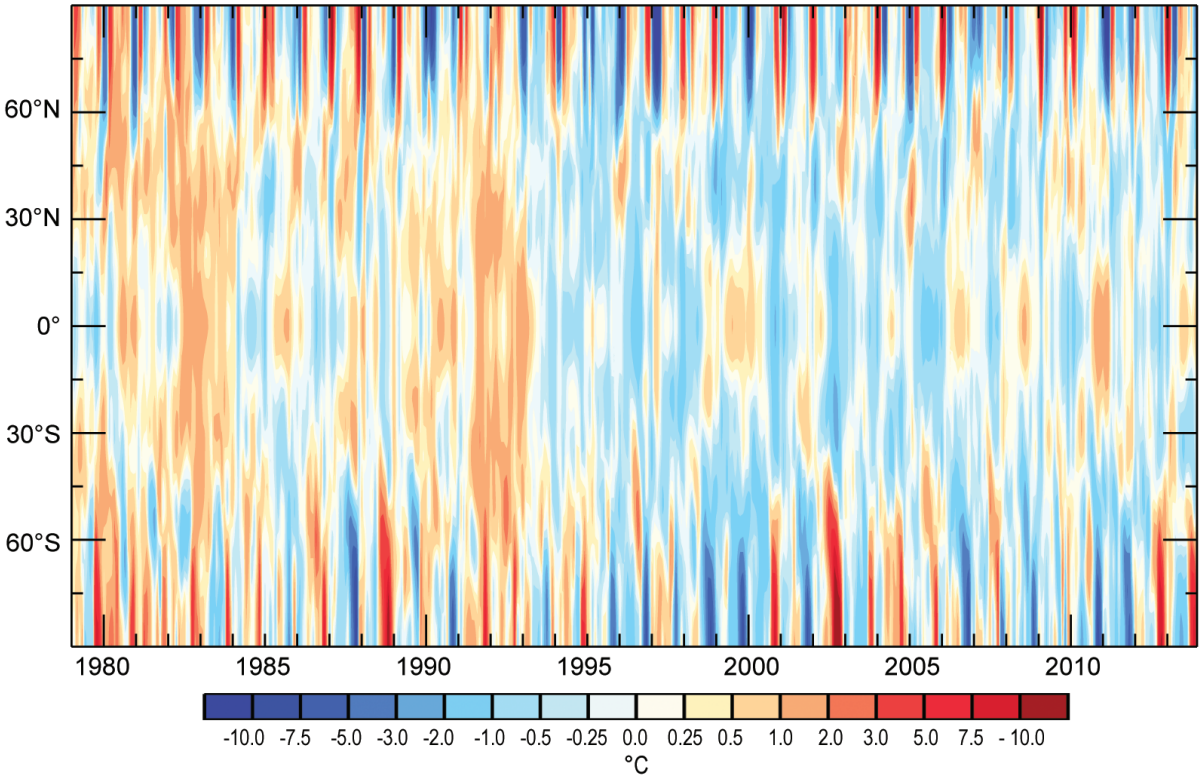

Fig. S2.4. ERA-Interim monthly mean anomalies (°C; 1981–2010 base period) of lower stratospheric temperature MSU Channel 4 equivalent by latitude.

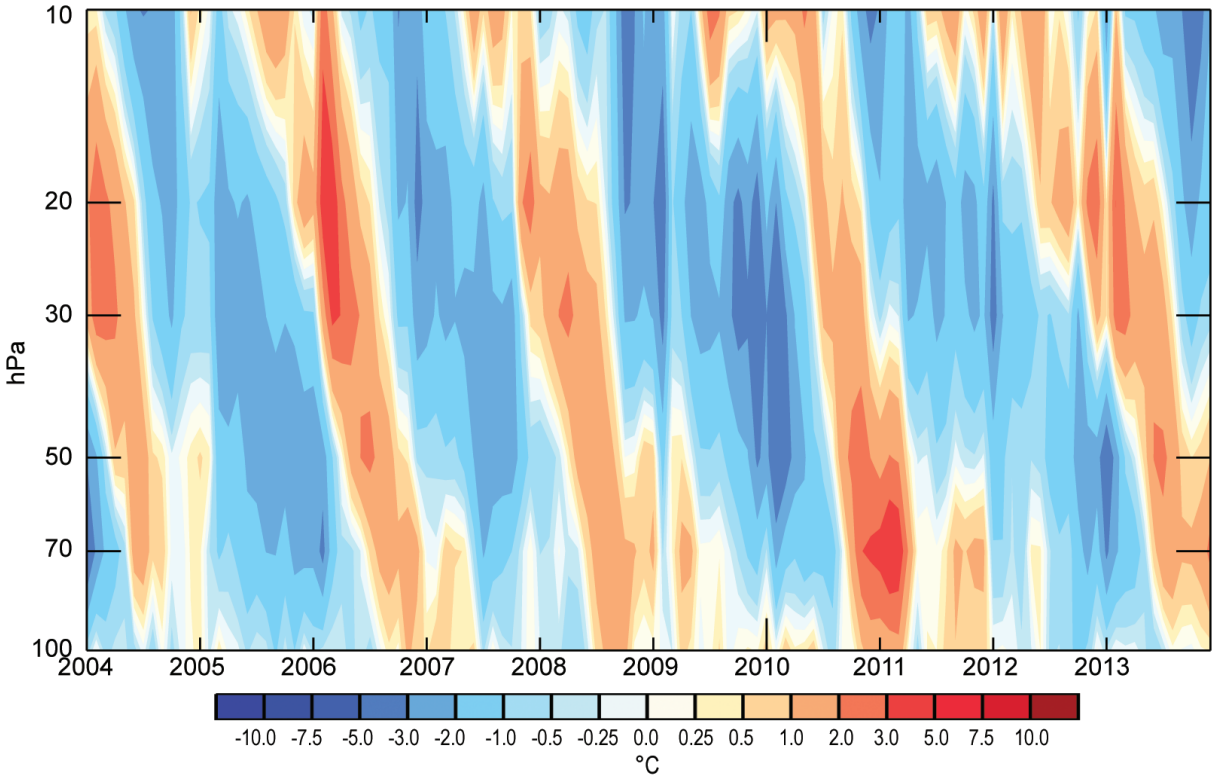

Fig. S2.5. Time-pressure analysis of MERRA equatorial lower stratospheric temperature anomalies (°C; 1981–2010 base period) from 100 to 10 hPa. Descending warm (cool) temperature anomalies coincide with descending westerly (easterly) quasi-biennial oscillating (QBO) winds.

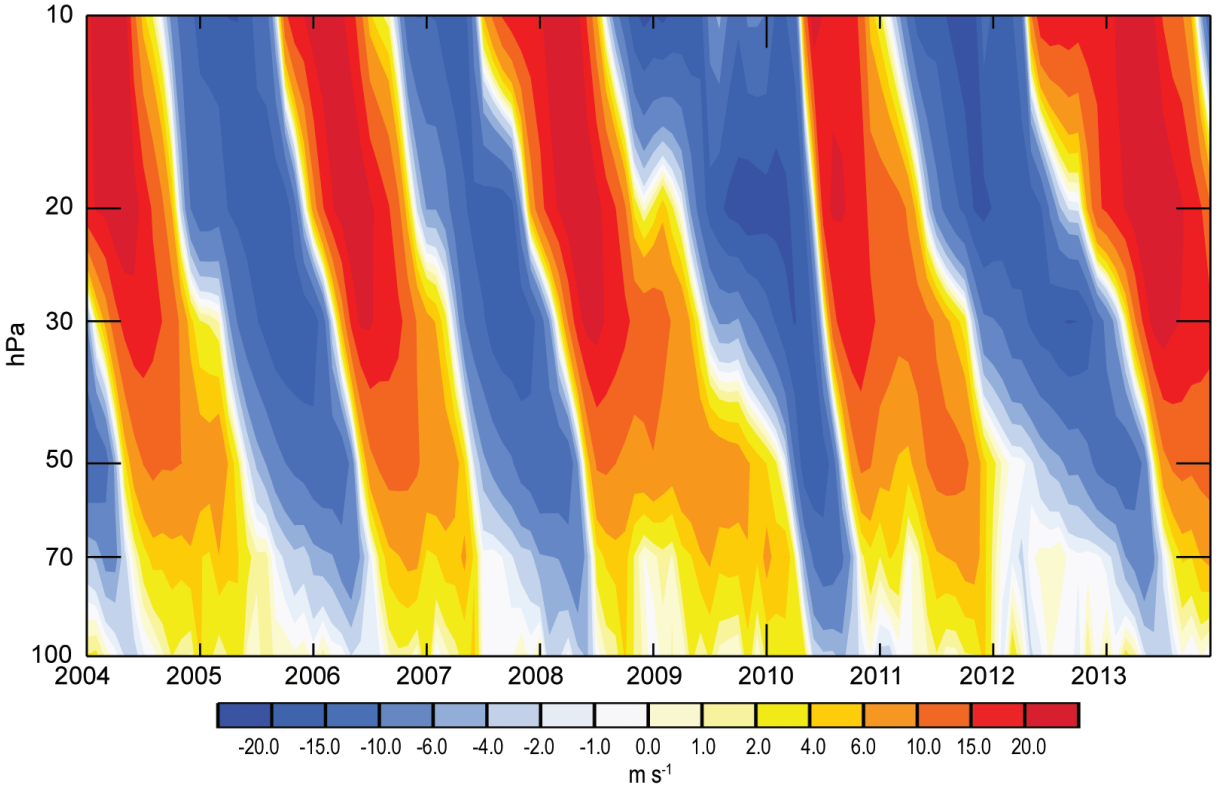

Fig. S2.6. Time-pressure analysis of MERRA reanalysis equatorial (10°S–10°N) lower stratospheric zonal wind anomalies (m s^{-1}; 1981–2010 base period) from 100 to 10 hPa. The descending quasi-biennial oscillating (QBO) winds were in descending westerly phase in 2013.

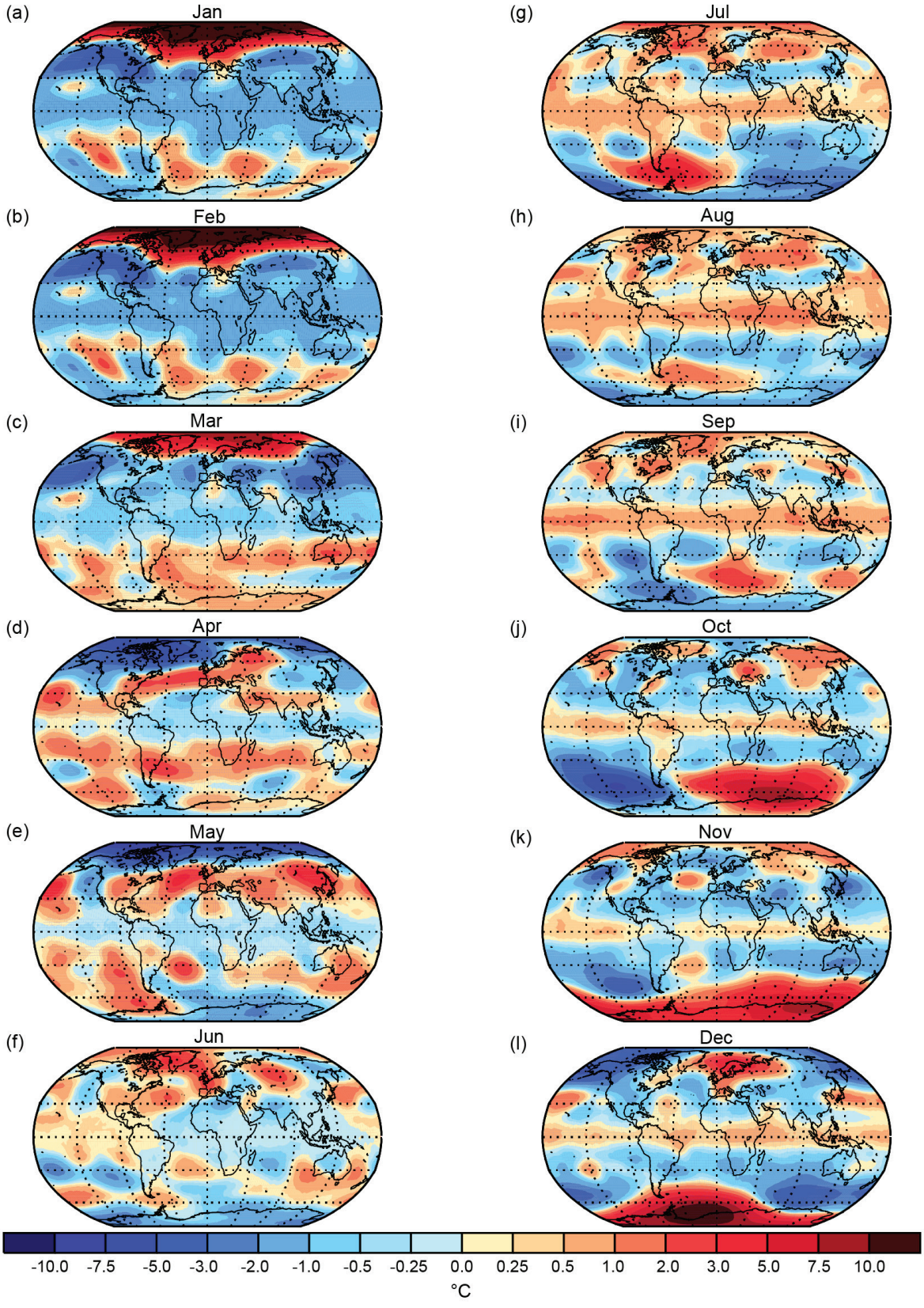

Fig. S2.7. MERRA monthly anomalies (°C, 1981–2010 base period) of MSU channel 4 equivalent layer for the lower stratospheric temperature for 2013.

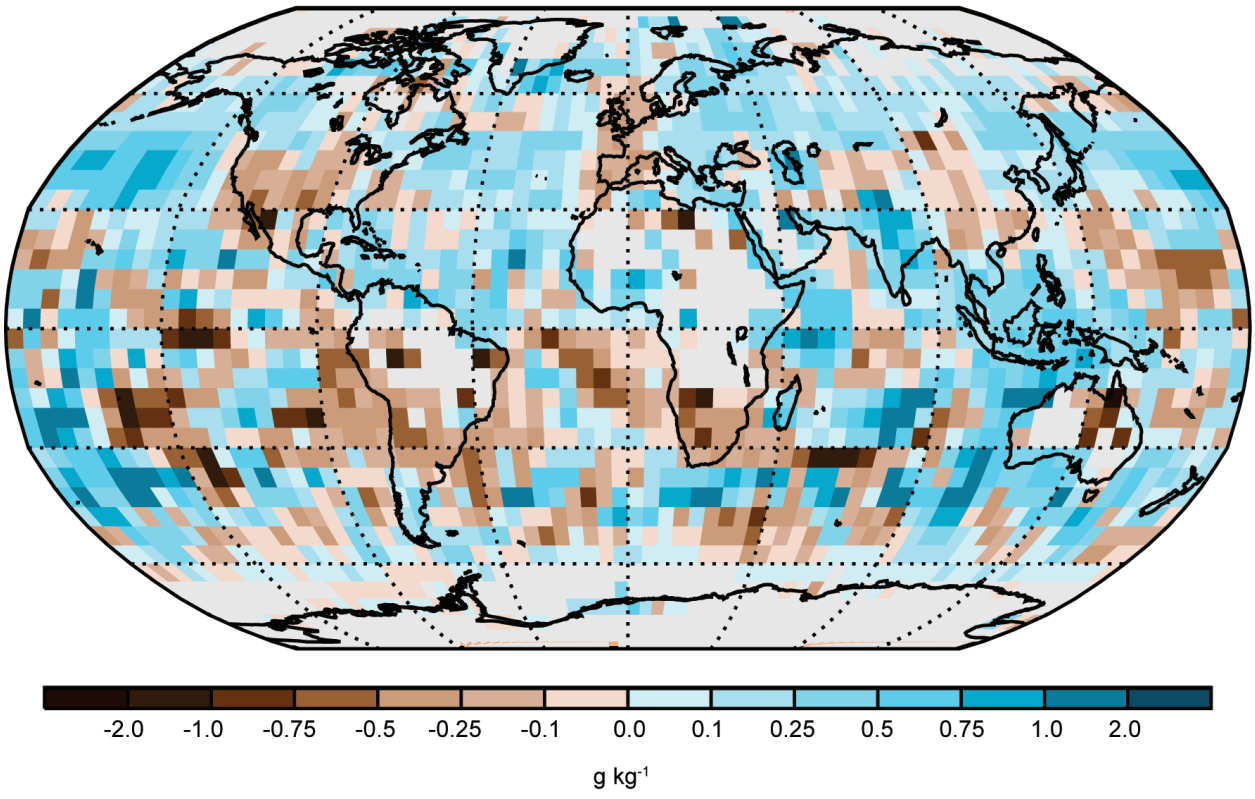

Fig. S2.8. Blended (NOCSv2.0 over oceans and HadISDH.2.0.0.2013p over land) 2013 annual anomalies for surface specific humidity (g kg^{-1}). Unlike Plate 2.1f, the complete NOCSv2.0 fields are used. Note that Plate 2.1f has been masked to only show regions where there is high confidence in the data quality.

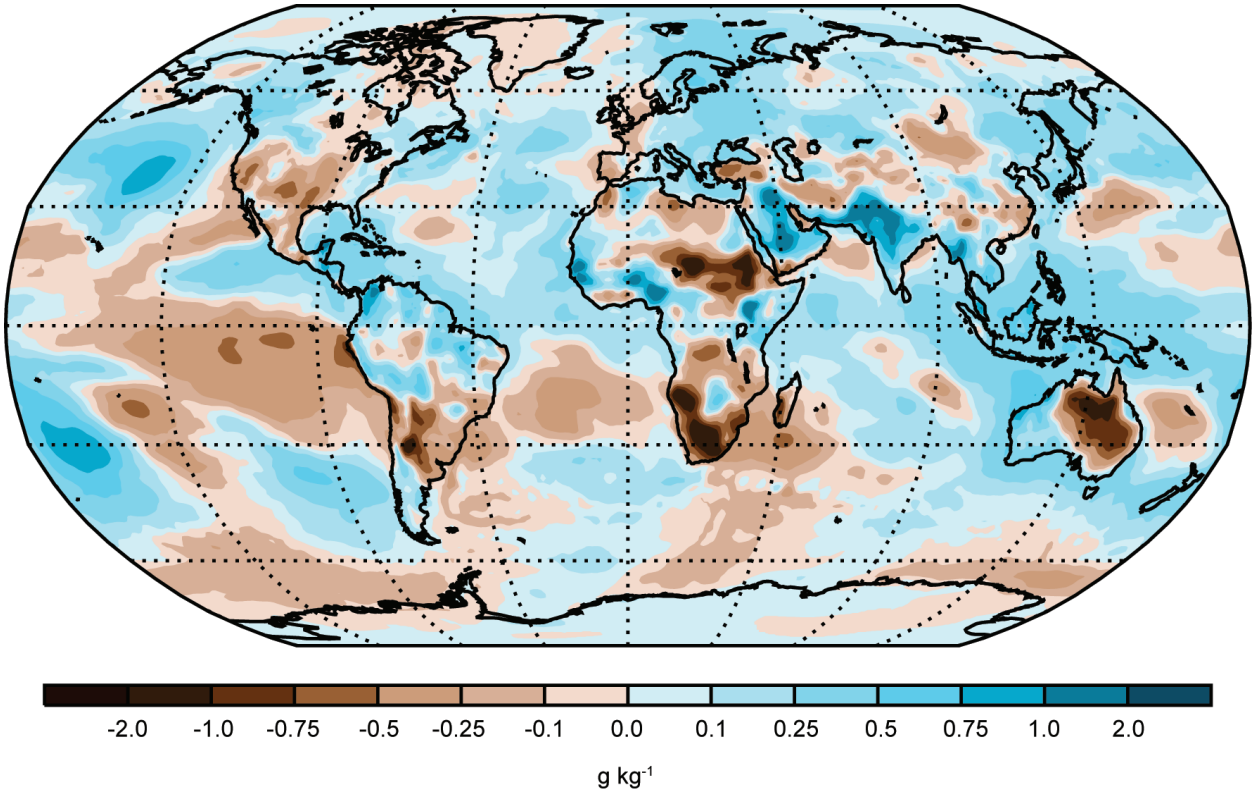

Fig. S2.9. ERA-Interim 2013 annual anomalies for surface specific humidity (g kg^{-1}).

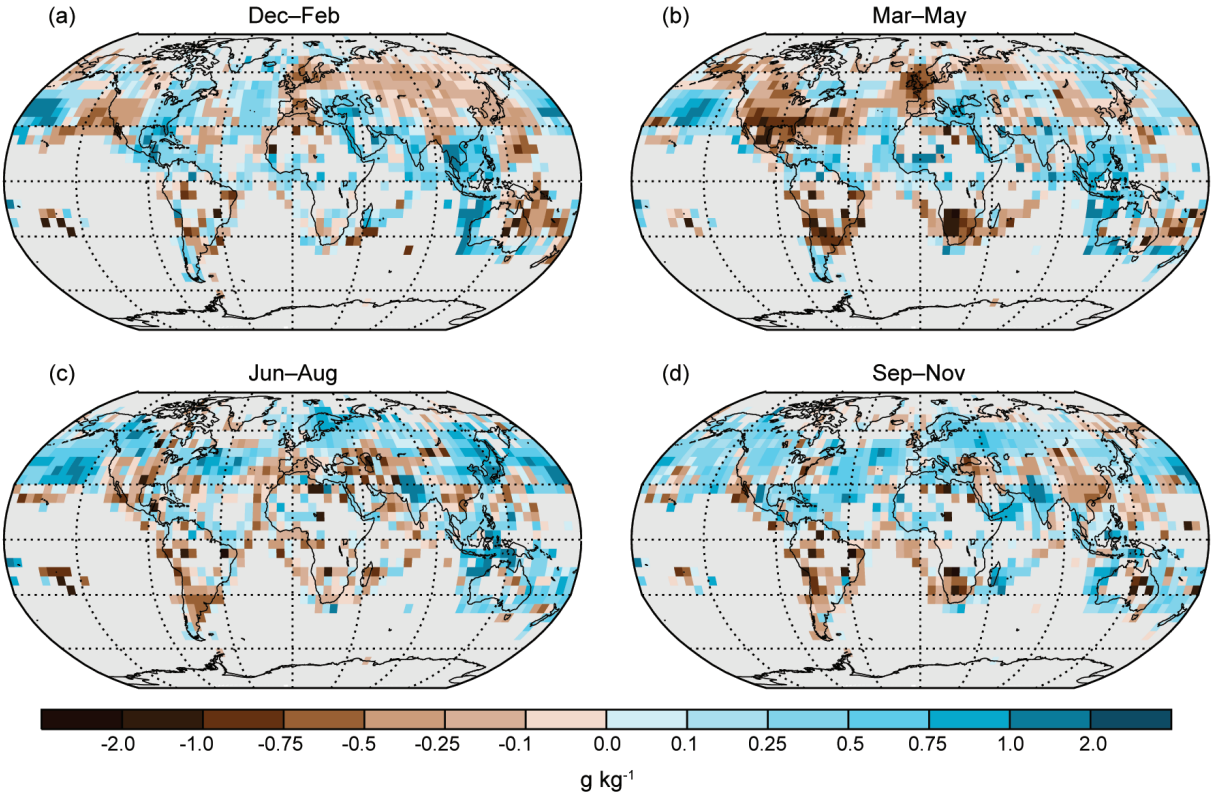

Fig. S2.10. Blended (NOCSv2.0 over oceans and HadISDH.2.0.0.2013p over land) 2013 seasonal anomalies for surface specific humidity (g kg^{-1}, 1981–2010 base period). For NOCSv2.0 (oceans) only data with high confidence in its quality are shown.

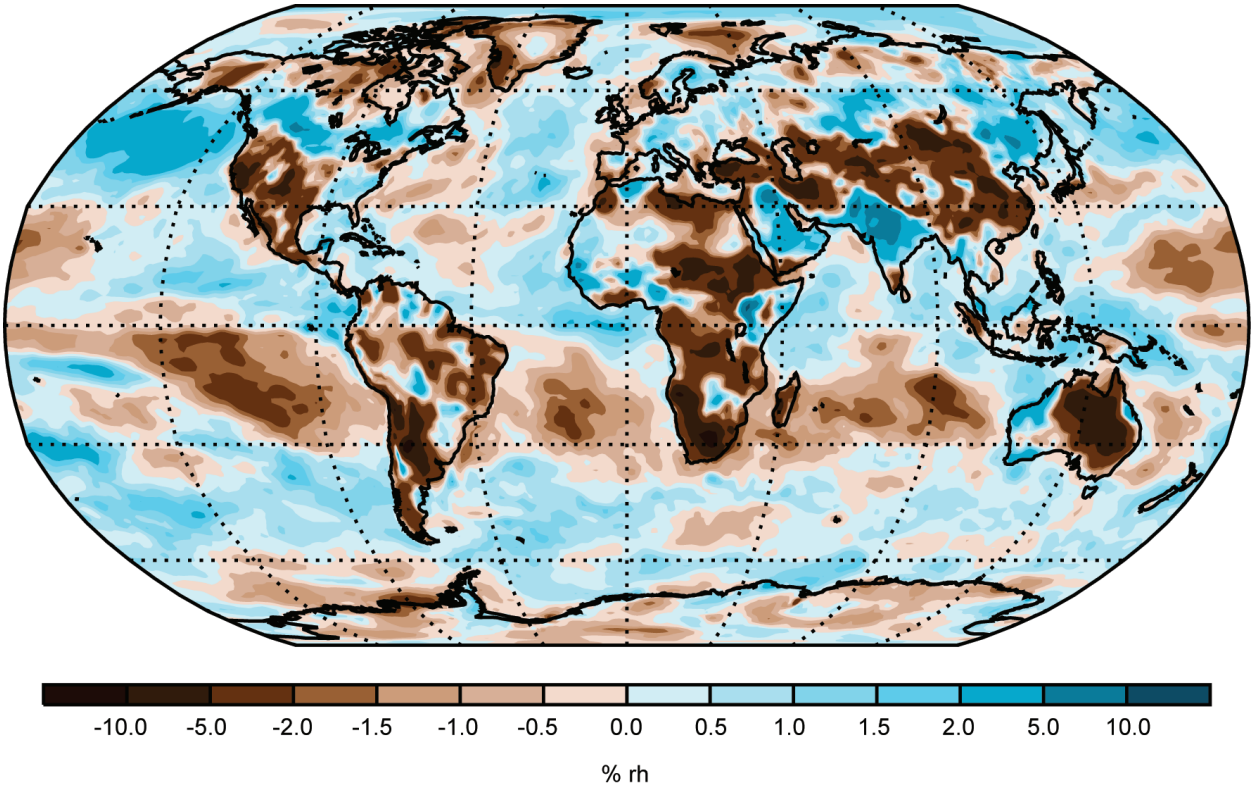

Fig. S2.11. ERA-Interim 2013 annual anomalies for surface relative humidity (%, 1981–2010 base period).

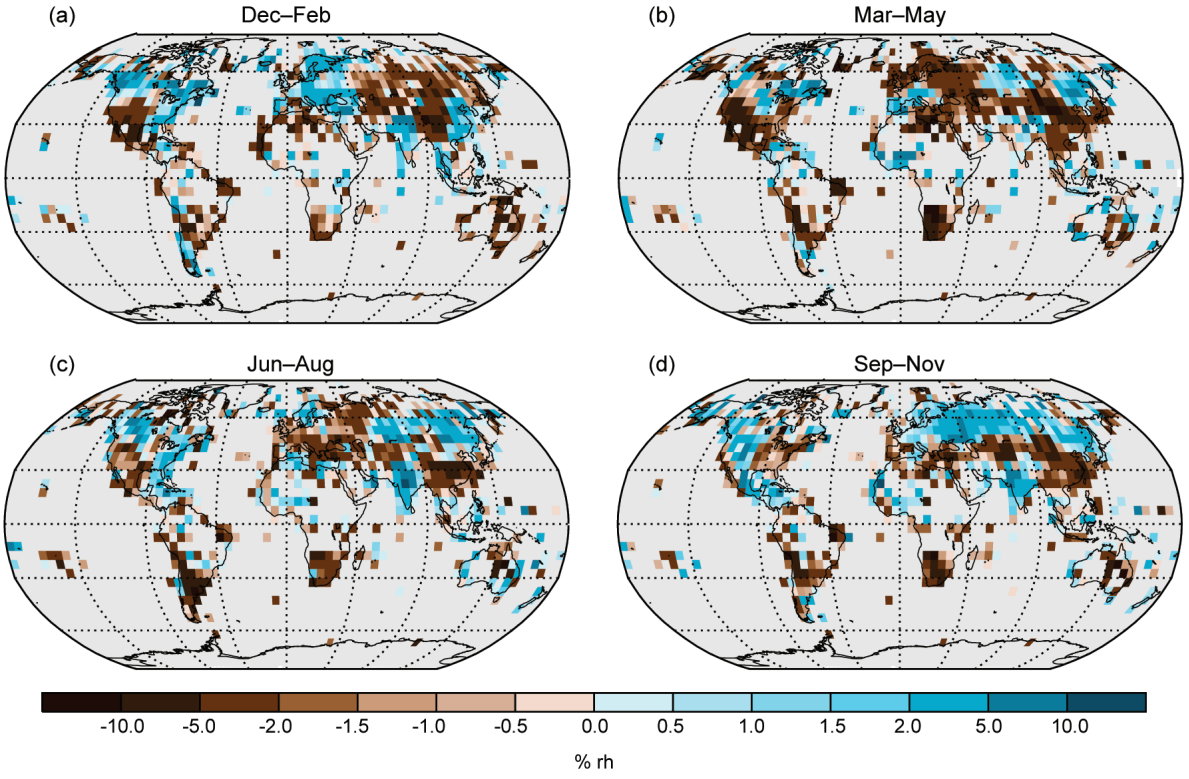

Fig. S2.12. HadISDH over land 2013 seasonal anomalies for surface relative humidity (%, 1981–2010 base period).

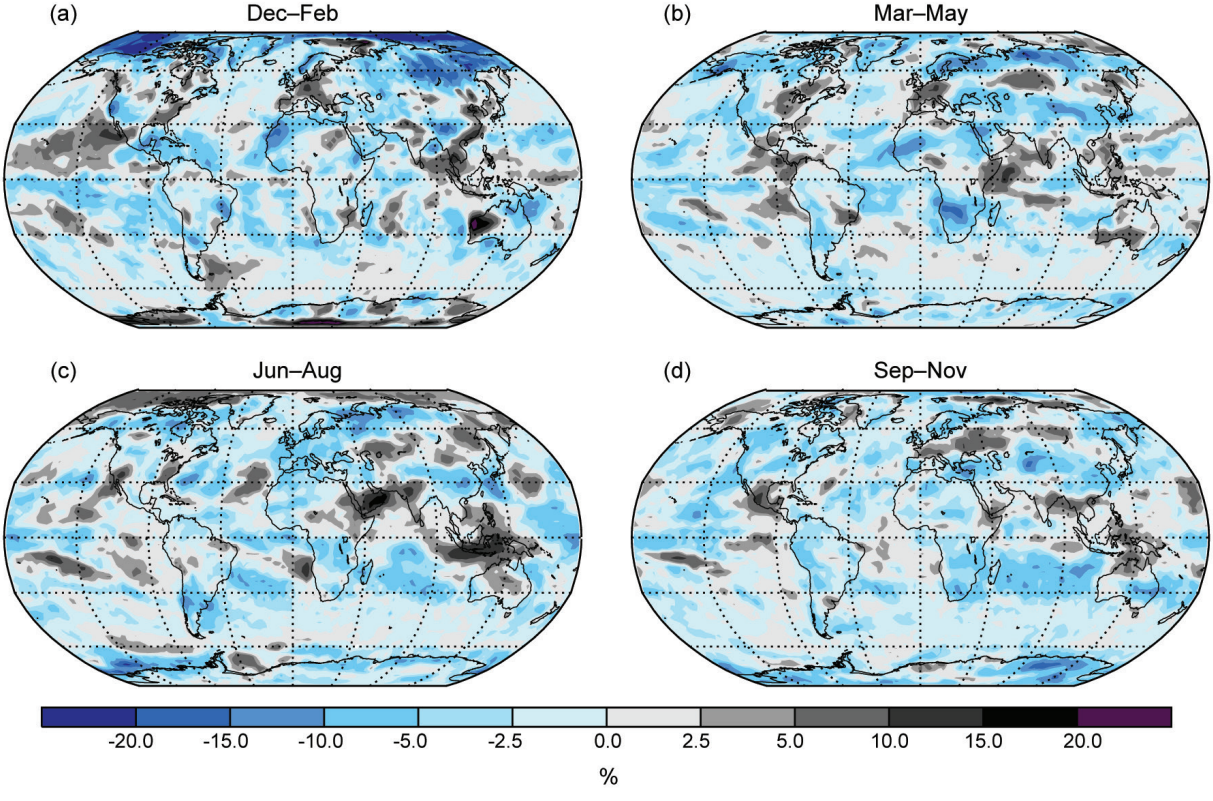

Fig. S2.13. Global cloudiness seasonal anomaly map (%) for 2013 generated from the 30-year PATMOS-x cloud climatology (1981–2010).

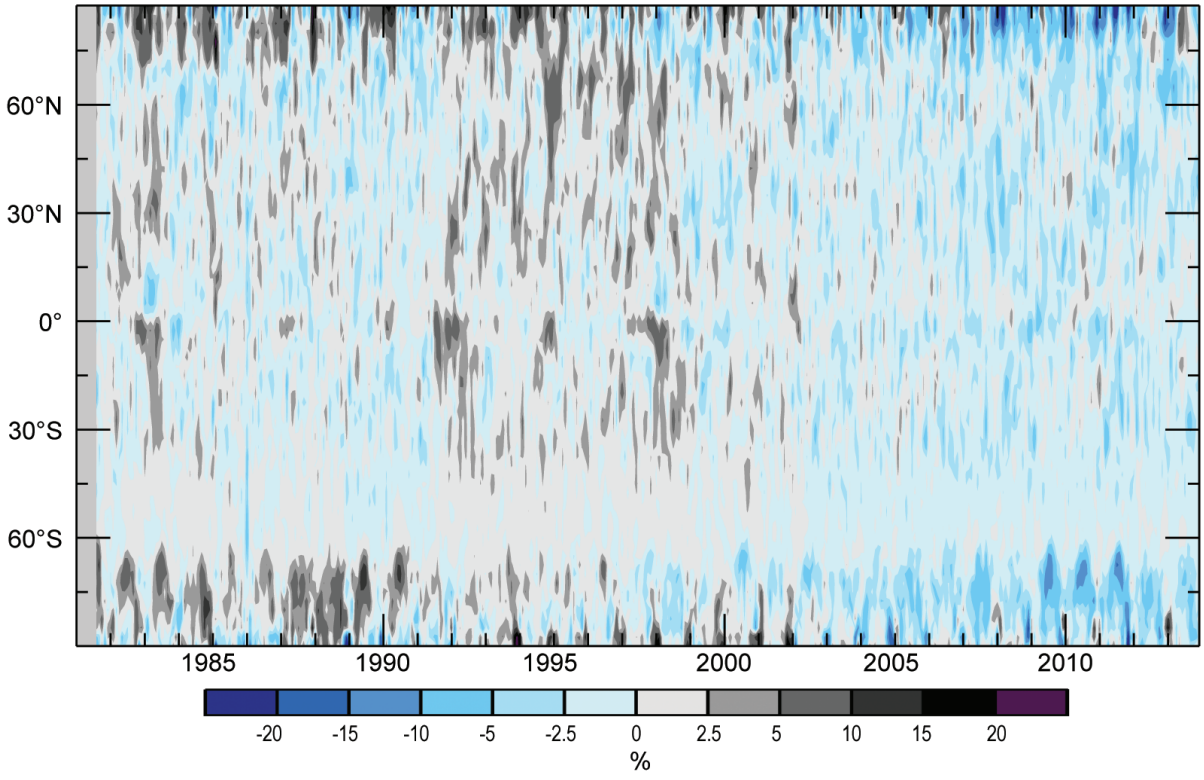

Fig. S2.14. PATMOS-x cloudiness monthly mean anomalies (%; 1981–2010 base period) averaged by latitude band.

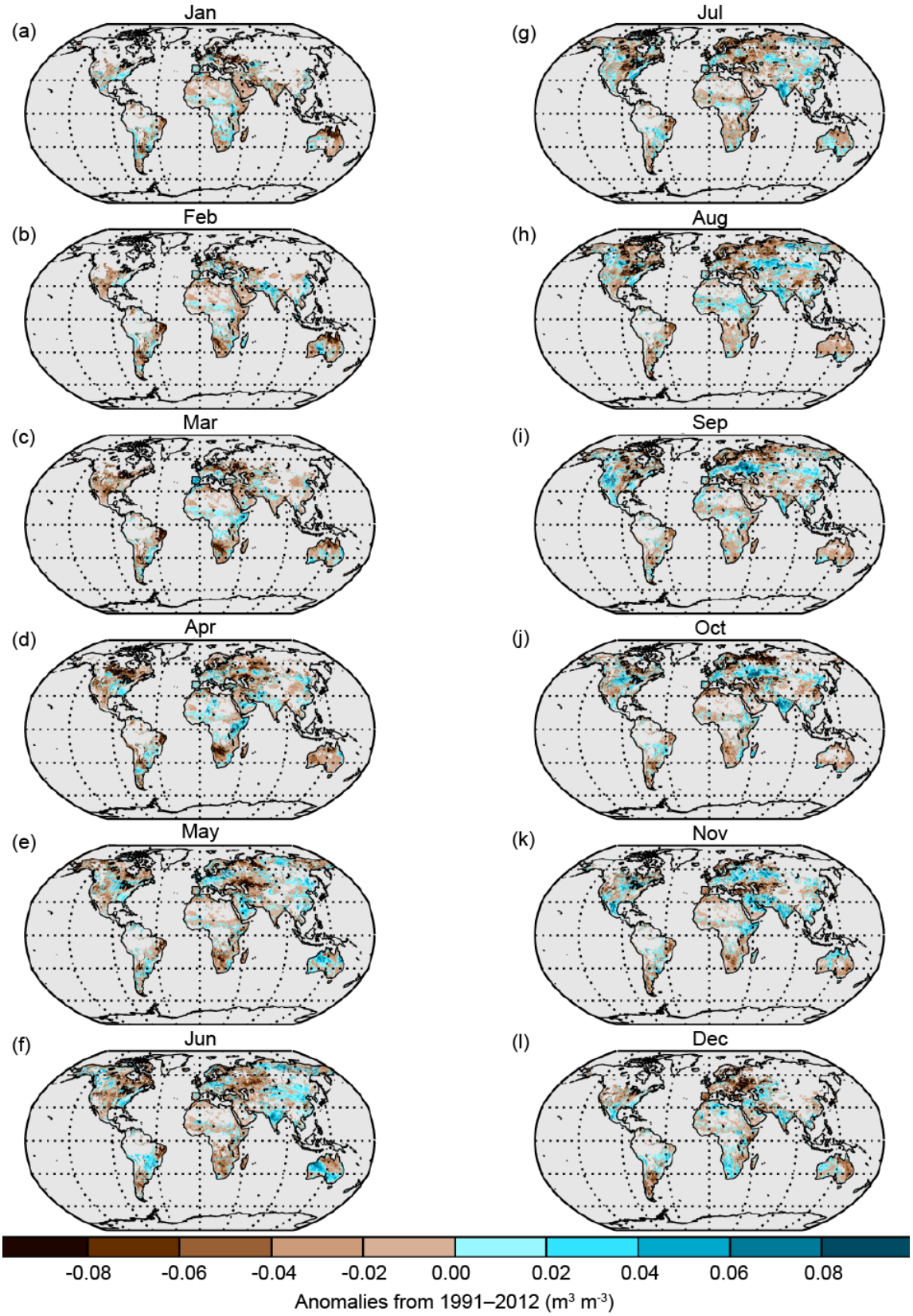

Fig. S2.15. Monthly soil moisture anomalies ($m^3\ m^{-3}$; 1991–2012 base period) for 2013 as calculated from ESA's CCI ESV soil moisture dataset.

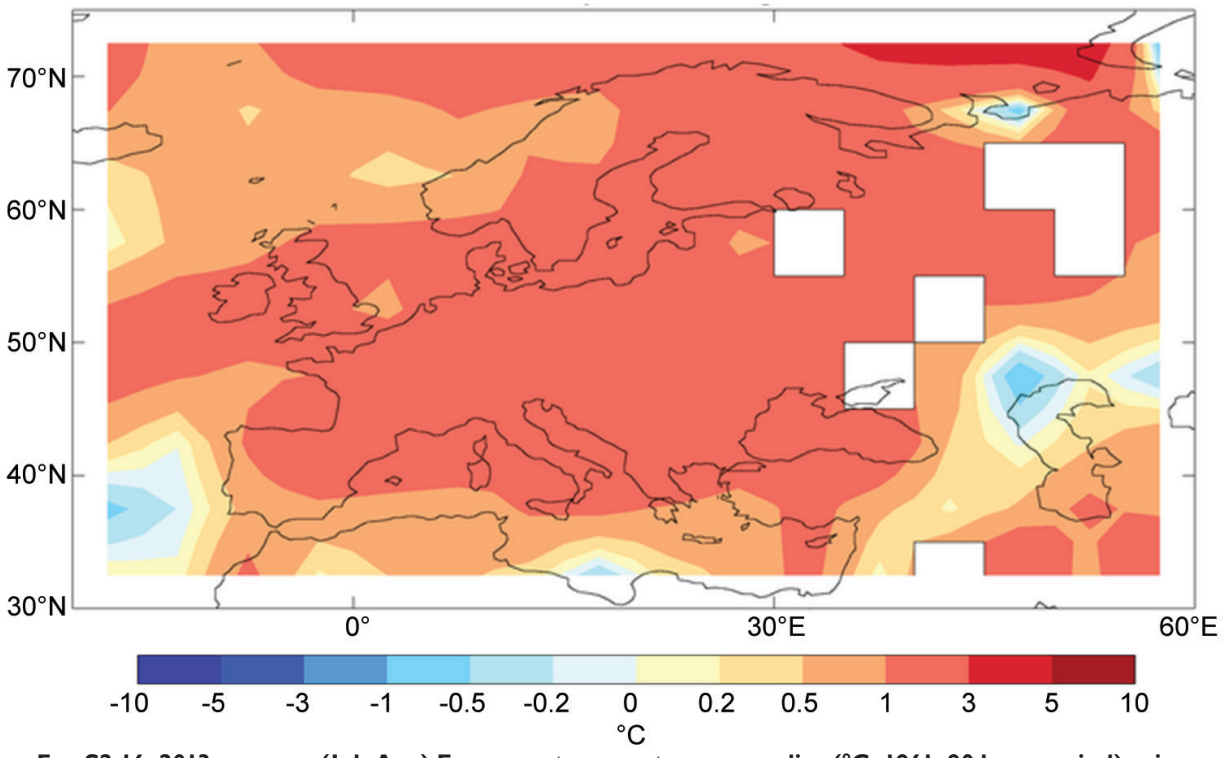

Fig. S2.16. 2013 summer (Jul–Aug) European temperature anomalies (°C; 1961–90 base period) using HadCRUT4.

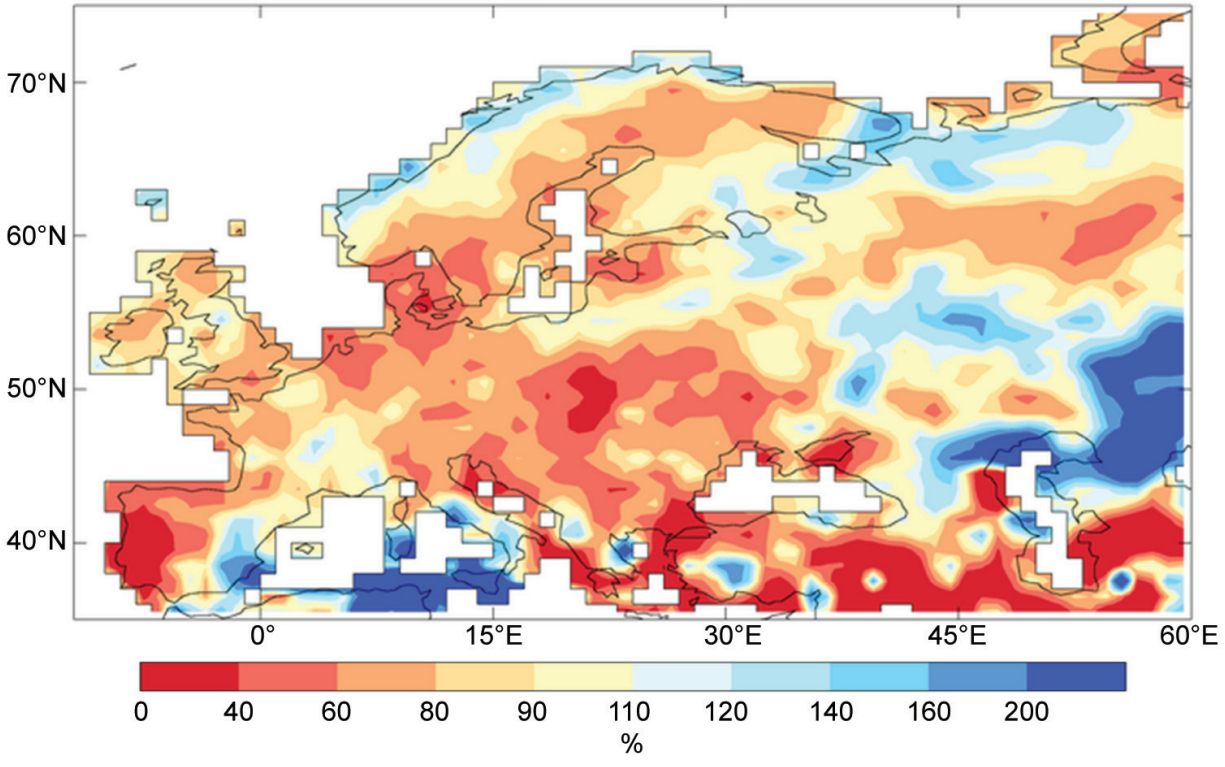

Fig. S2.17. 2013 summer (Jul–Aug) European rainfall anomalies (%; 1961–90 base period) using provisional GPCP data.

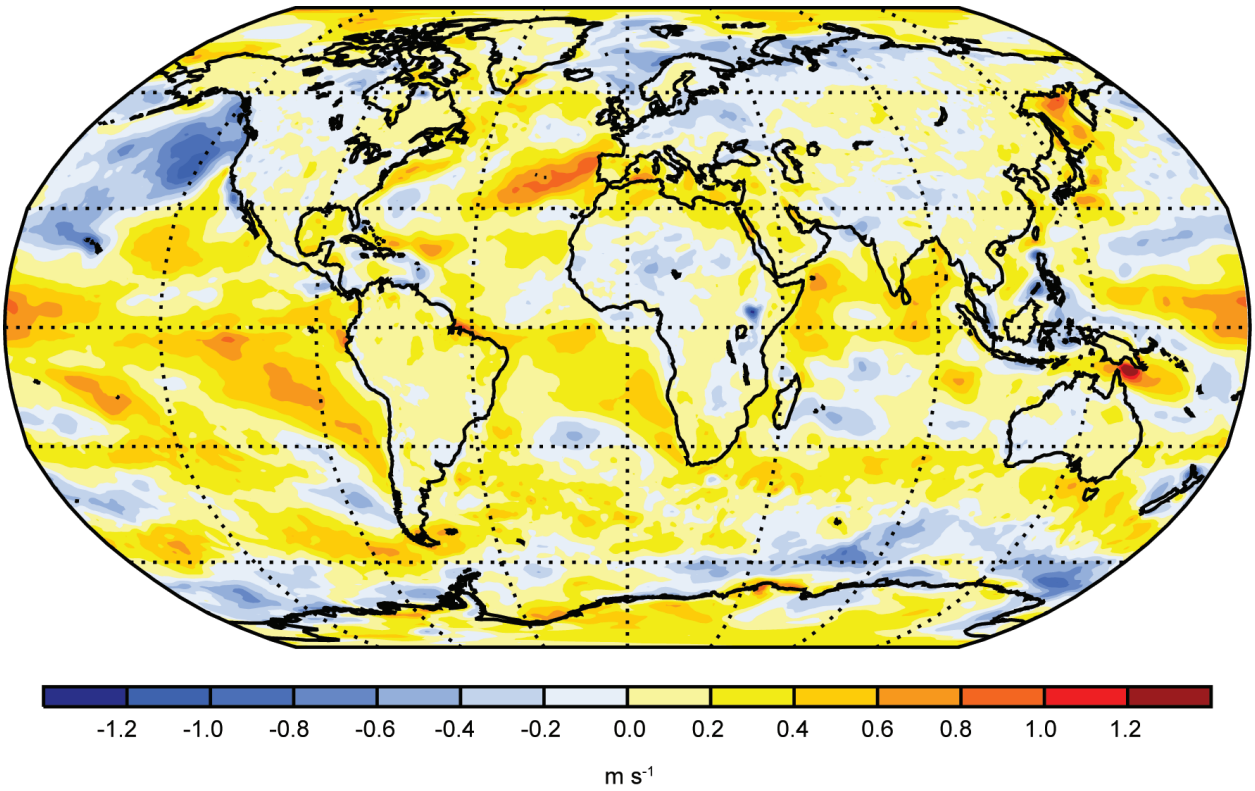

Fig. S2.18. ERA-Interim (grids) and ISD-Lite (land points) 2013 annual anomalies (m s^{-1}; 1981–2010 base period) for land surface wind speed.

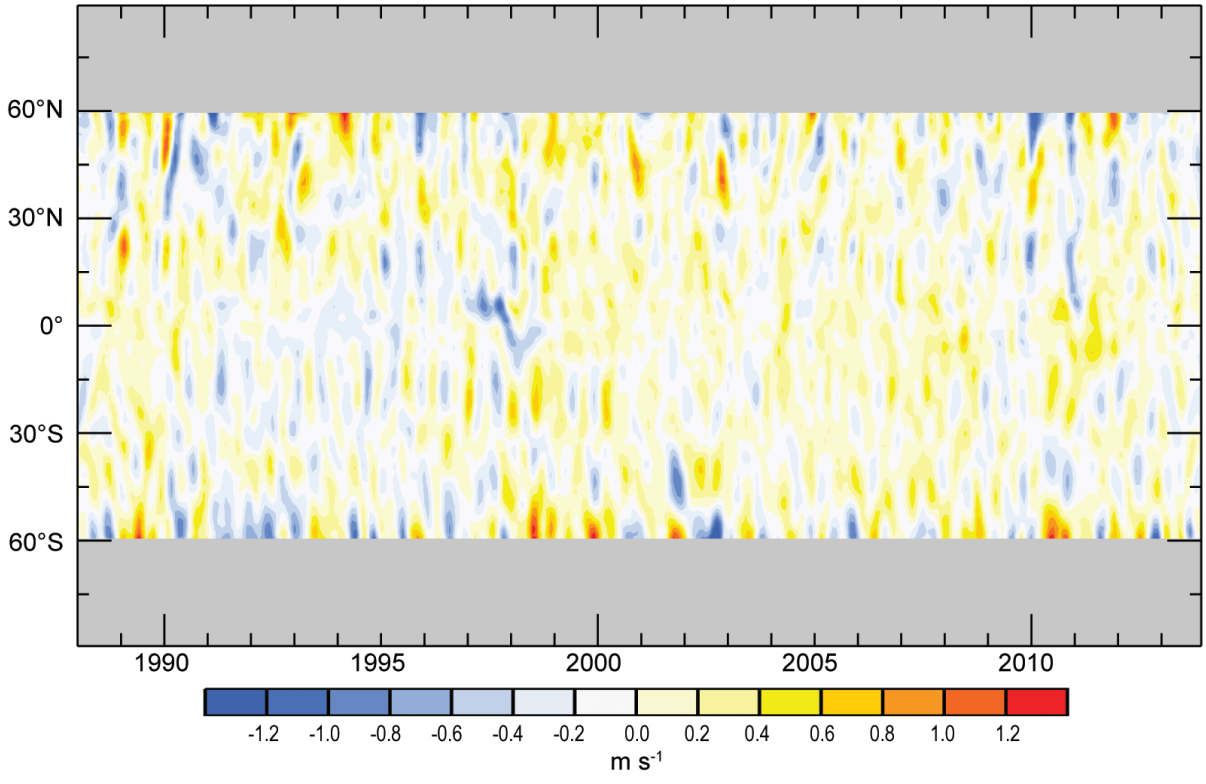

Fig. S2.19. Zonally-averaged monthly mean surface wind speed anomalies (m s^{-1}; reference period 1988–2010) over the ice-free oceans. Data have been smoothed in time to remove variability on time scales shorter than four months.

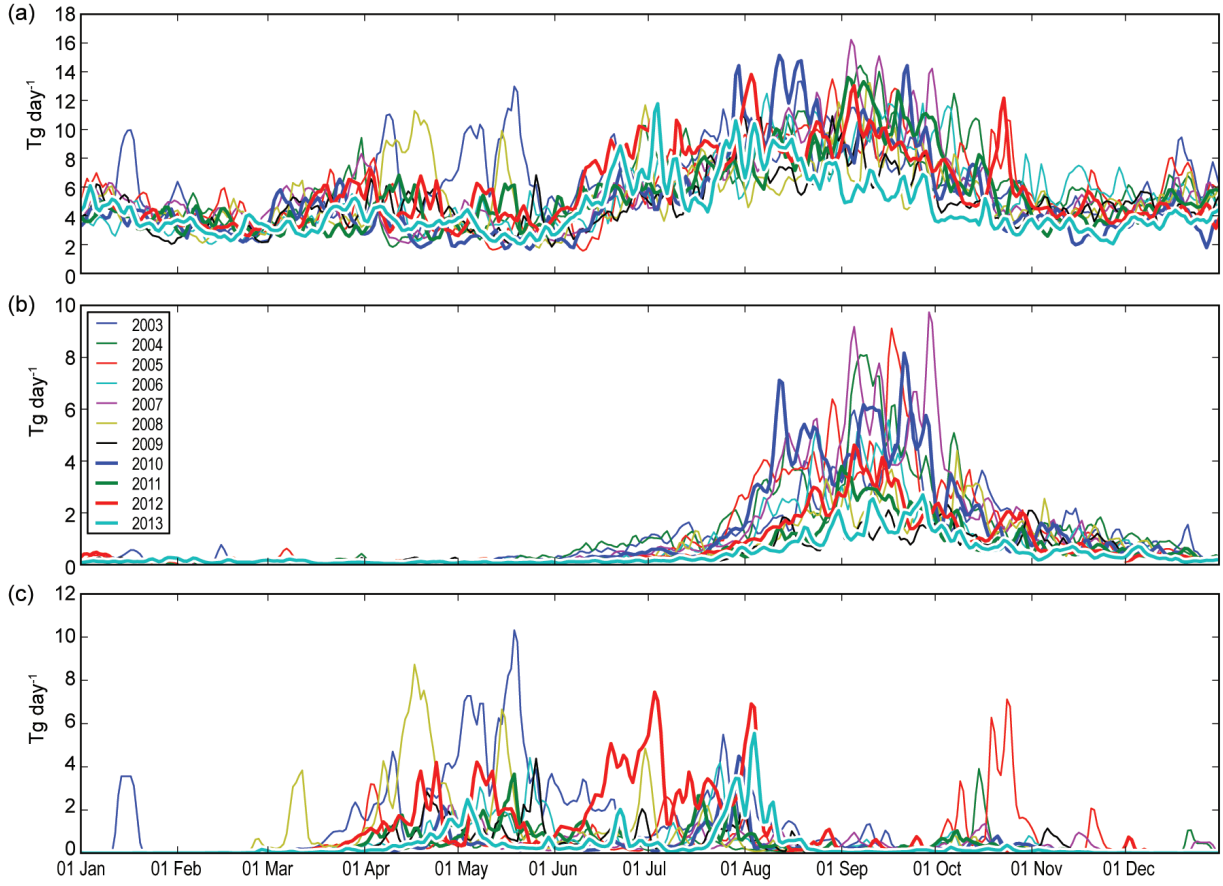

Fig. S2.20. Daily fire activity in terms of carbon consumption (Tg C day^{-1}) (a) globally and for (b) Southern Hemisphere America, and (c) Northern Asia, covering 2003–13 from GFASv1.0 inventory.

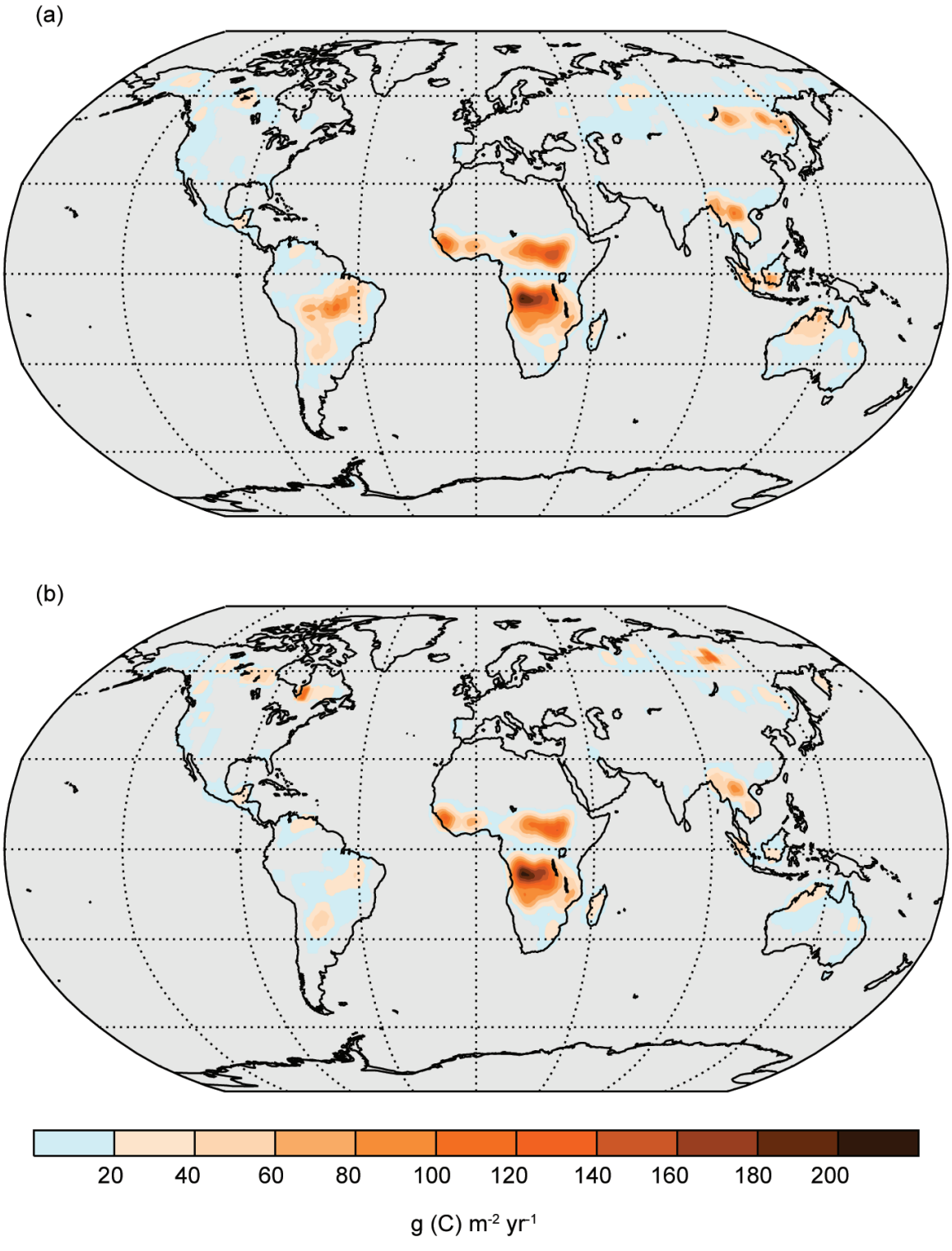

Fig. S2.21. MACC GFASv1.0 global maps of biomass burning in terms of carbon emission (g C m^{-2} yr^{-1}) during (a) 2003–12 and (b) 2013. The map projection highlights high latitudes.

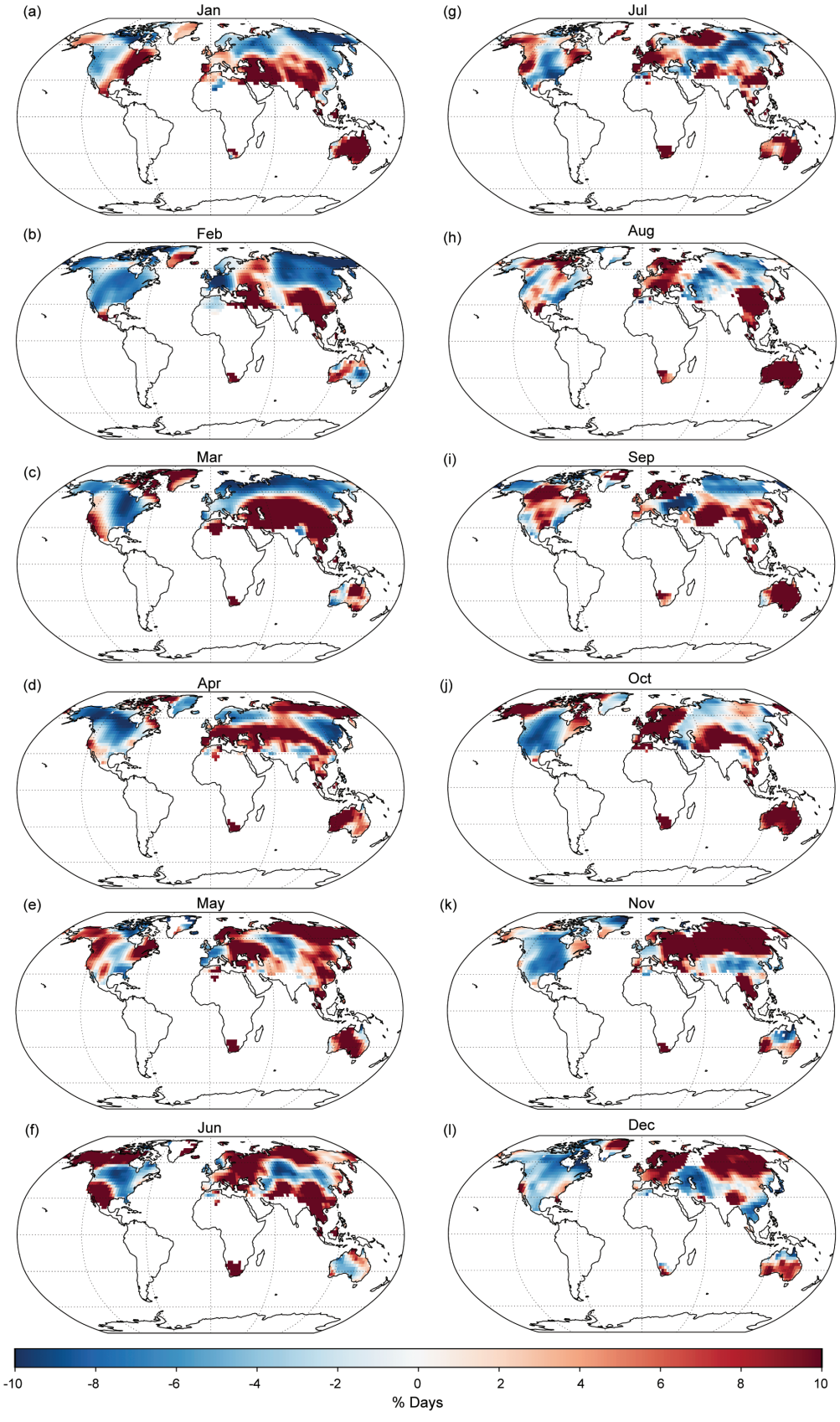

Fig. SB2.1. GHCNDEX 2013 monthly anomalies (% days; 1961–90 base period) for TX90p (warm days).

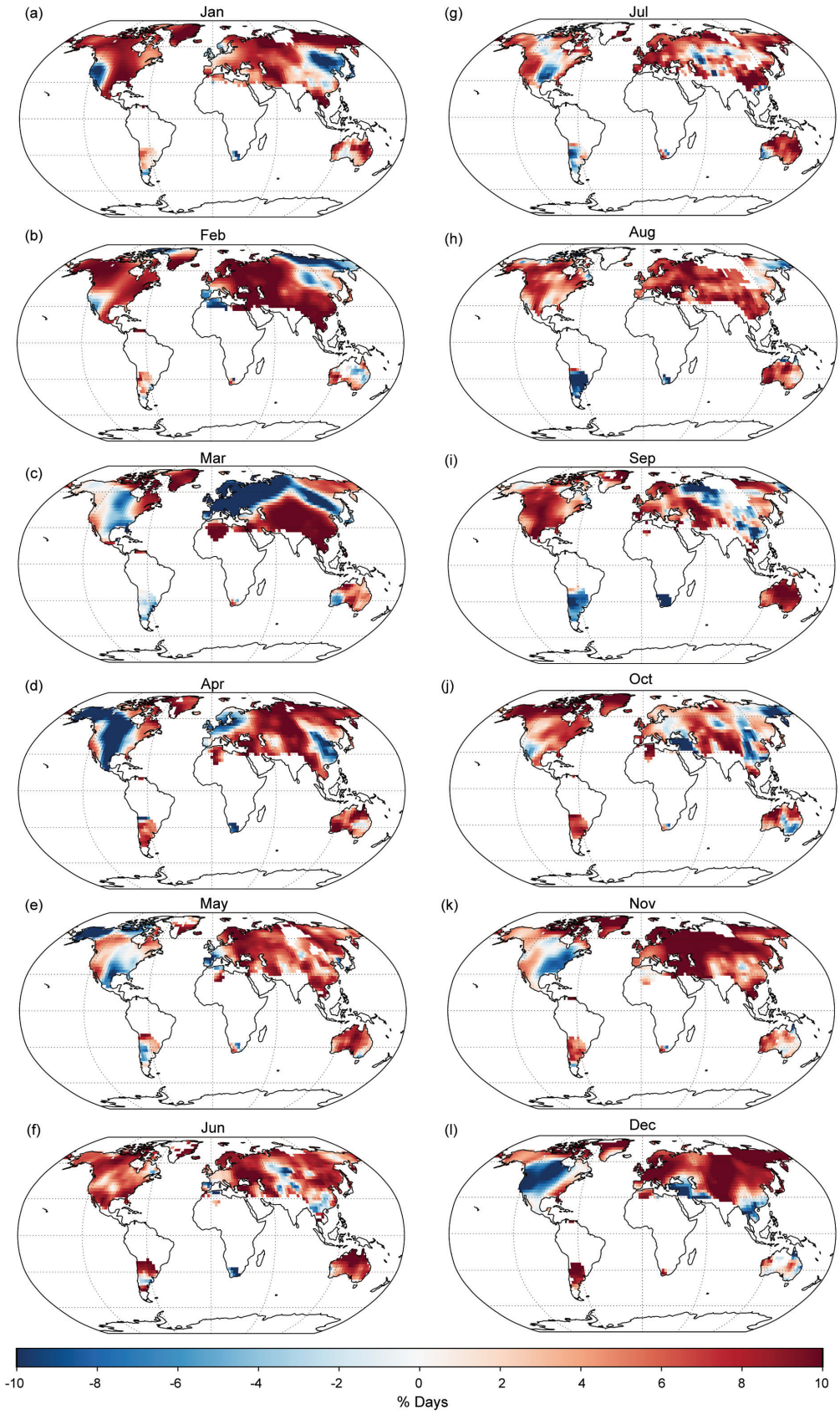

Fig. SB2.2. GHCNDEX 2013 monthly anomalies (% days; 1961–90 base period) for TN10p (cool nights).

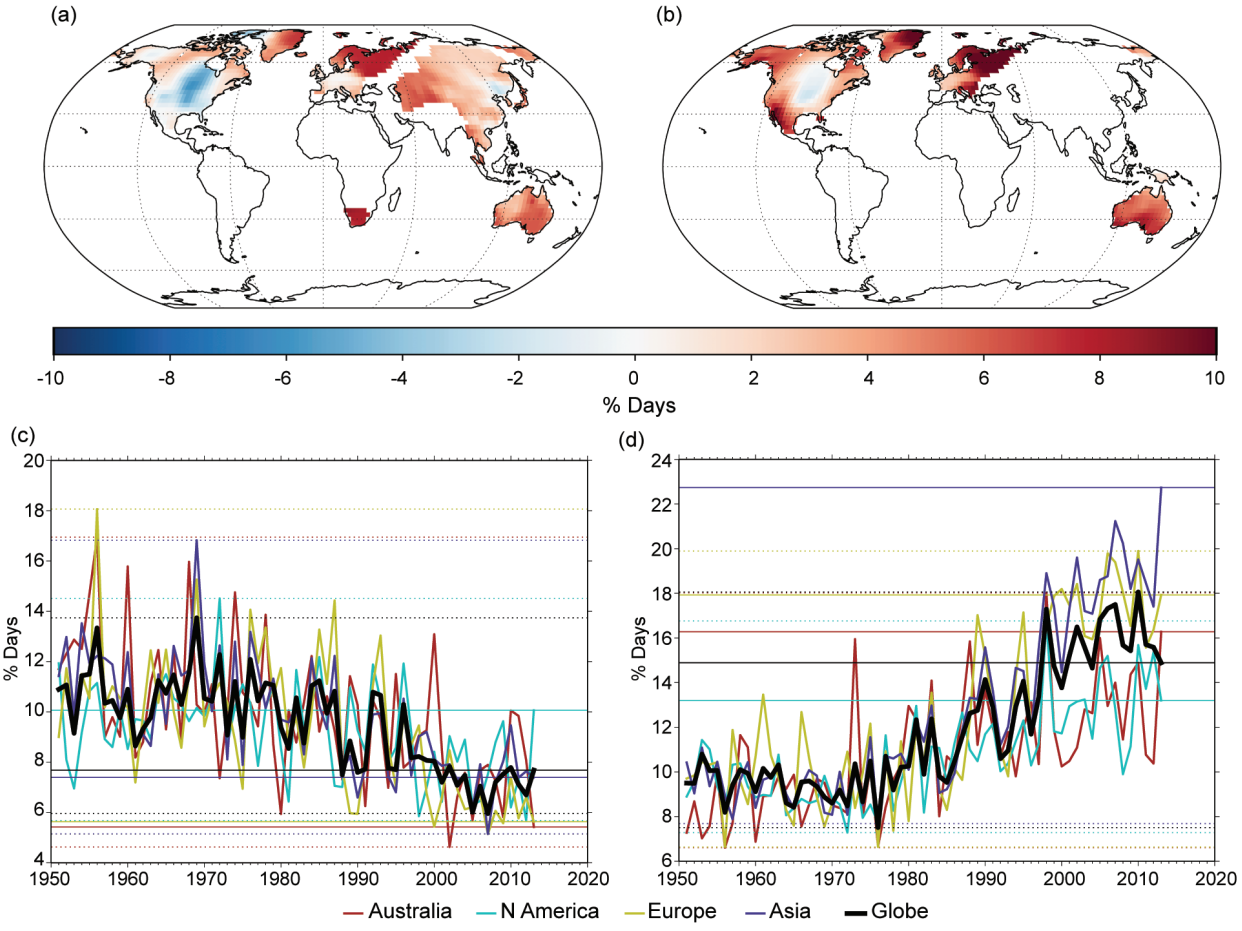

FIG. SB2.3. GHCNDEX TX10p and TN90p anomaly maps and time series relative to the 1961–90 base reference period. (a) TX10p (cool days) and (b) TN90p (warm nights) anomalies for 2013 (% days). Note change in direction of color scale (red indicates warmer than normal, blue cooler than normal). (c) TX10p and (d) TN90p area-average time series for Australia, North America, Europe, Asia, and the globe. Dotted horizontal lines show the values of the record maximum and minimum. The solid horizontal lines show the value for 2013. Only grid boxes which have data for 90% of the years since 1950 are included when calculating the global average.

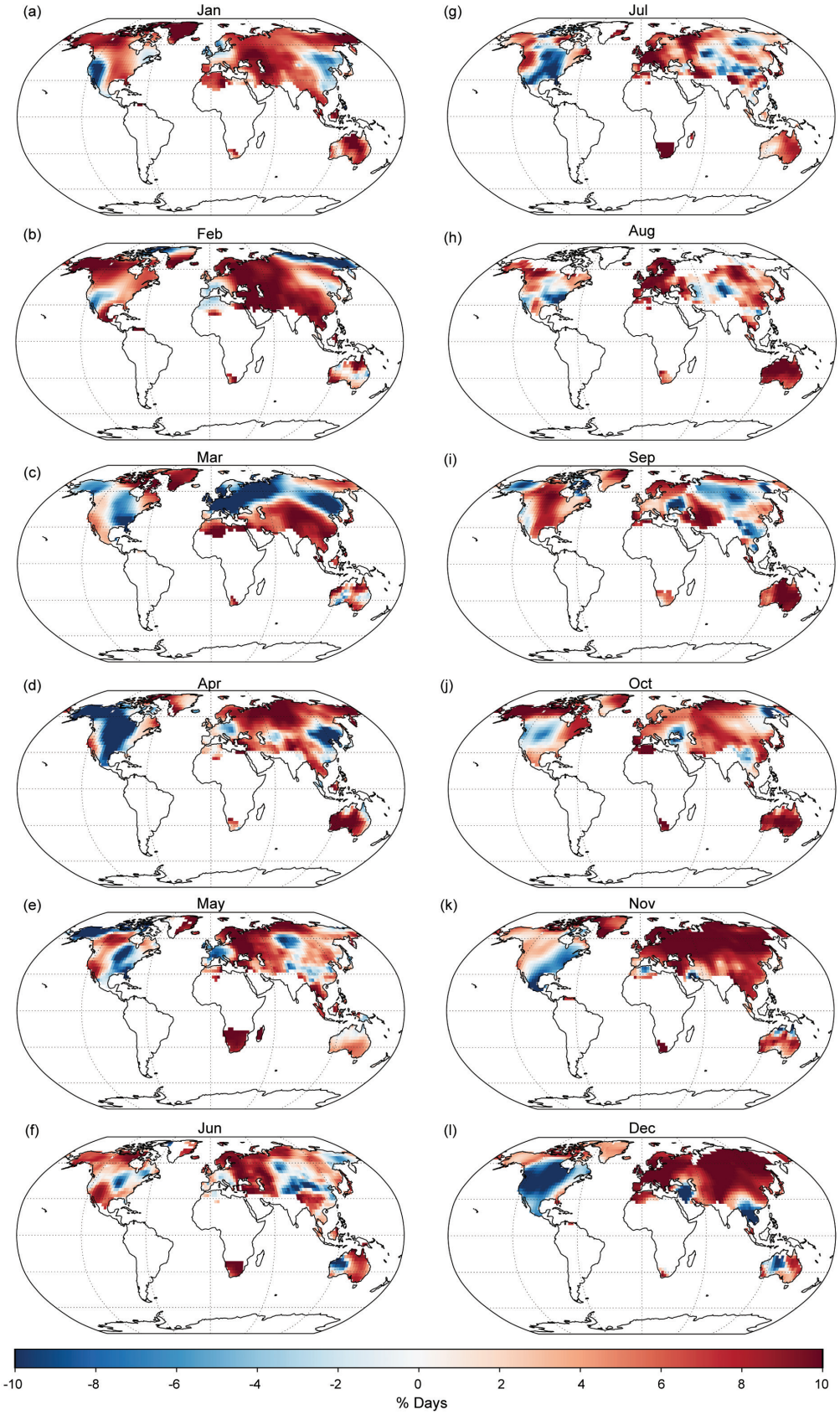

Fig. SB2.4. GHCNDEX 2013 monthly anomalies (% days; 1961–90 base period) for TX10p (cool days).

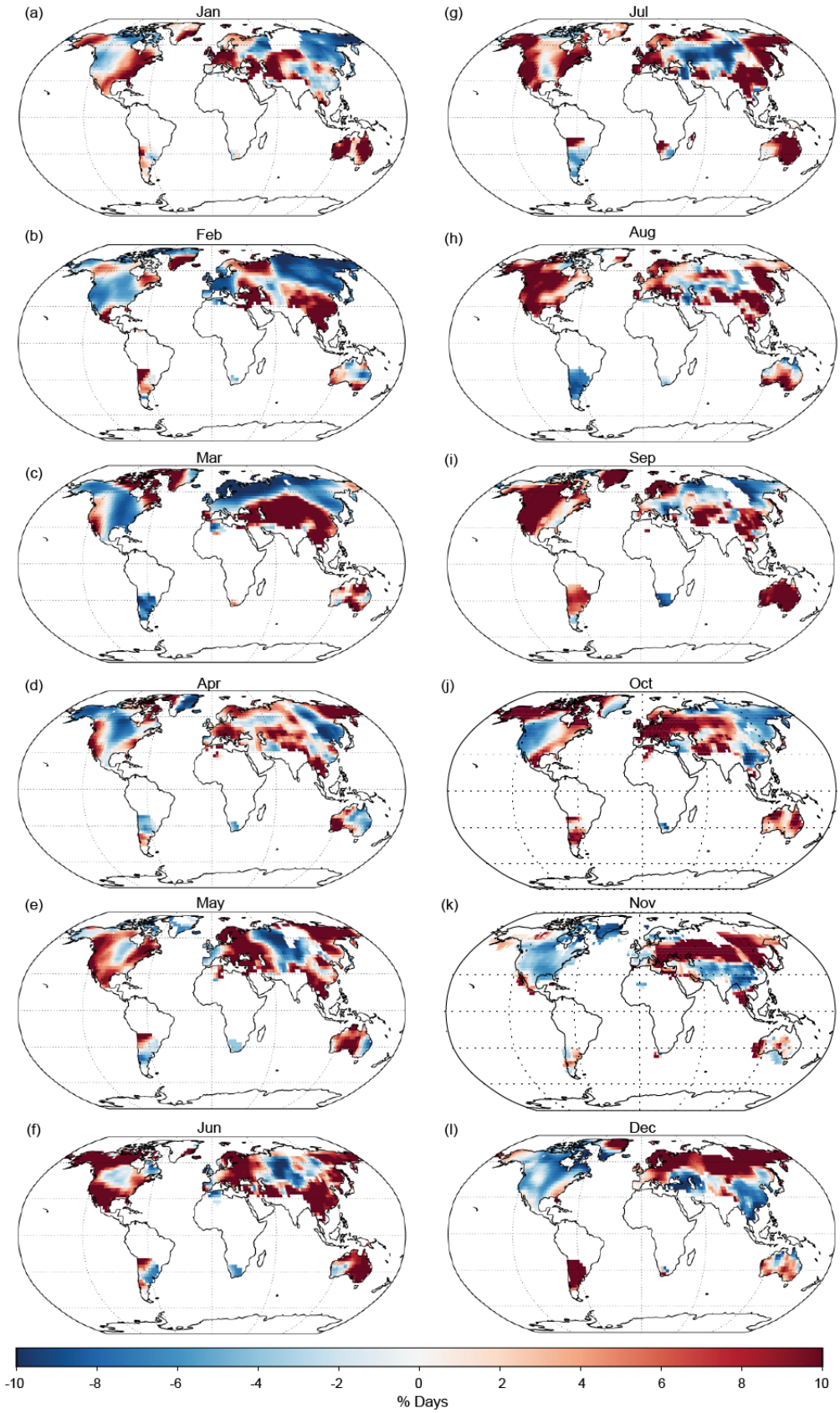

Fig. SB2.5. GHCNDEX 2013 monthly anomalies (% days; 1961–90 base period) for TN90p (warm nights).

Please Note:

Due to a coding error in the merging algorithm, the original anomaly data after 2002 have an average negative offset of about 0.003 $m^3 m^{-3}$. This has been corrected in the following updated figures from the full report.

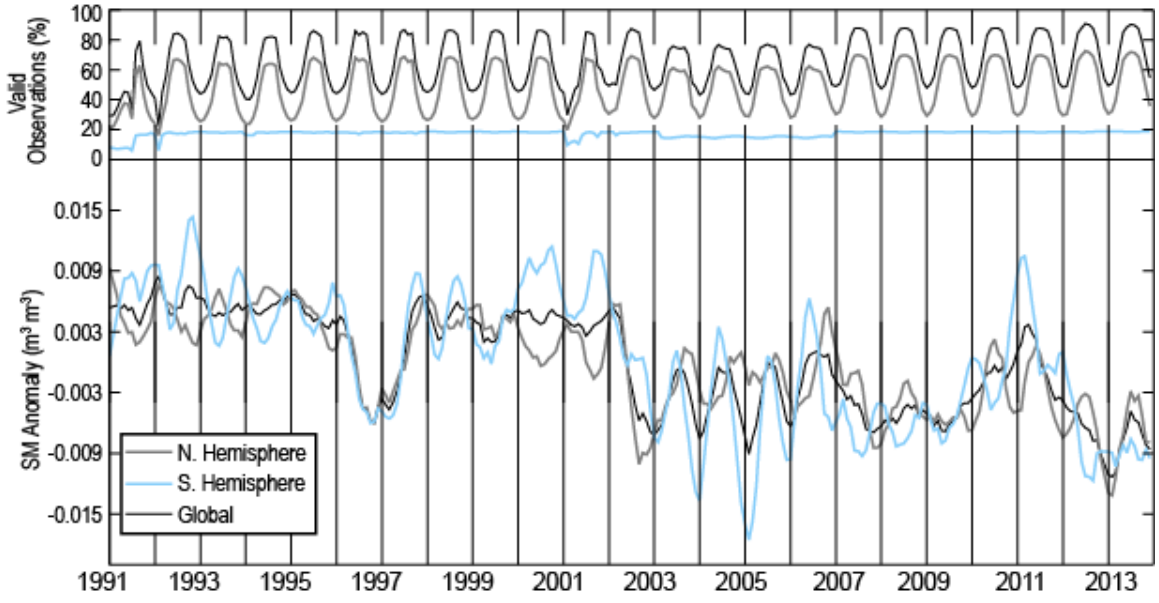

Fig. 2.21. ESA's CCI ECV SM time series of average global soil moisture anomalies ($m^3 m^{-3}$) for the period 1991–2013 (relative to the 1991–2012 base period). The top plot shows the percentage of land pixels with valid observations.

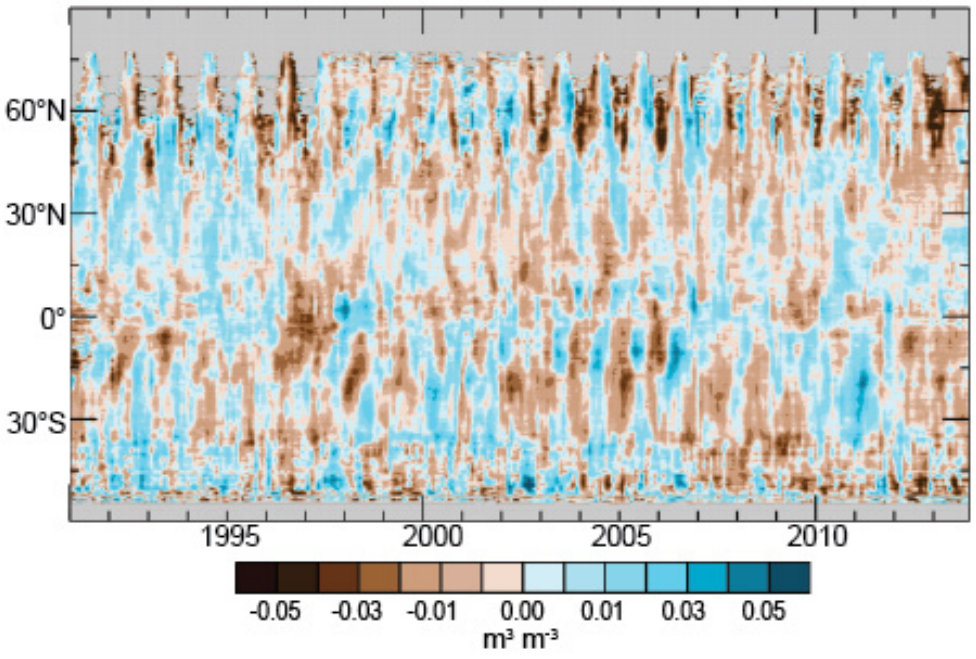

Fig. 2.22. Time-latitude diagram of ECV soil moisture anomalies ($m^3\ m^{-3}$) with respect to baseline period 1991–2012

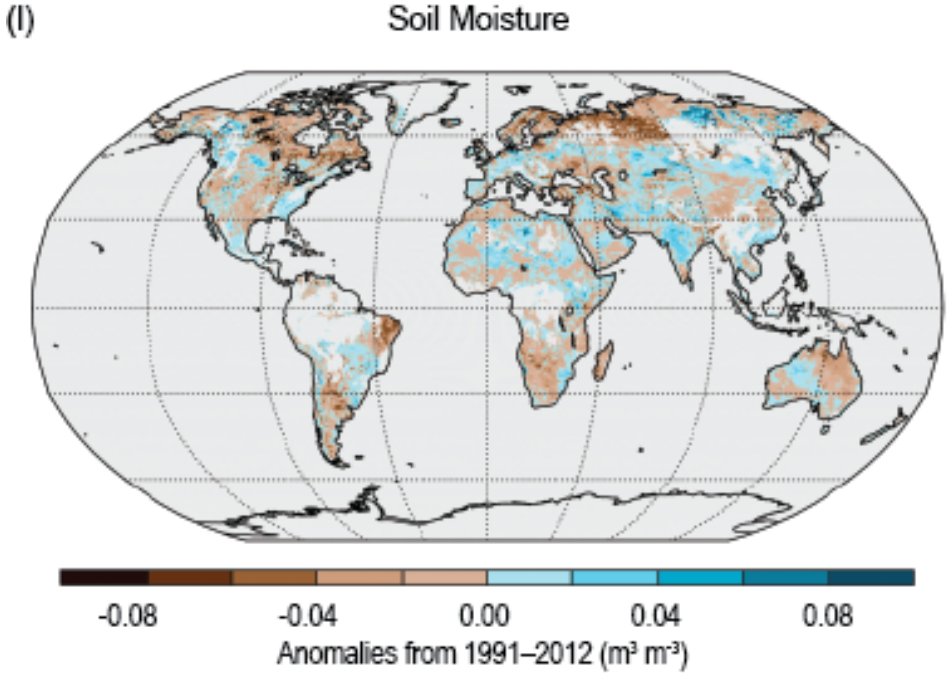

Plate 2.1. Annually-averaged global spatial anomaly maps for many of the ECVs presented in this chapter.
(One section-l only)
(l) ESA CCI ECV SM 2013 anomalies of soil moisture.